Solid State Phenomena
ISSN: 1662-9779, Vol. 387, pp 103-117
doi:10.4028/p-sDKXB6

Submitted: 2026-01-19
Revised: 2026-02-16
Accepted: 2026-02-20
Online: 2026-04-14

A CT-Based Methodology for Mesostructural Characterization of Unidirectional Continuous-Fiber Polymer Composites Using Line-Profile Descriptors

MELE Roberto[1,a*], DE SIO Paolo[1,b], TUCCI Fausto[1,c]
and CARLONE Pierpaolo[1,d]

[1]Department of Industrial Engineering, University of Salerno, 132 Via Giovanni Paolo II, 84084 Fisciano (SA), Italy

[a]rmele@.unisa.it, [b]pdesio@unisa.it, [c]ftucci@unisa.it, [d]pcarlone@unisa.it

Keywords: X-ray micro-computed tomography, unidirectional continuous- fiber composites, mesostructure characterization, line-profile features.

Abstract. X-ray micro-computed tomography enables three-dimensional inspection of fiber-reinforced polymer composites. Quantitative mesostructural characterization remains challenging when voxel size does not permit reliable phase segmentation. This study presents a CT-based methodology for mesostructural characterization of unidirectional continuous-fiber polymer composites using line-profile descriptors. The approach extracts fixed one-dimensional intensity profiles within a defined internal volume of interest and computes a compact set of statistical and spatial descriptors. These include distributional moments, entropy, gradient-based measures, autocorrelation-derived correlation length, spectral band-energy ratios, and percentile-based run-length metrics. A technical quality control procedure verifies numerical consistency of the extracted feature tables. A one-at-a-time sensitivity analysis quantifies the influence of descriptor hyperparameters and identifies parameter groups that alter signal partitioning, particularly spectral cut-offs and run-length thresholds. Applied to pultruded composites, the descriptors resolve transverse heterogeneity across the section and systematic through-thickness trends in attenuation level, dispersion, spatial scale, and persistence of low-attenuation domains. The methodology provides a traceable low-dimensional representation of attenuation structure that can inform finite-element modeling through spatially parameterized material fields. Mechanical validation and descriptor–property calibration remain subjects for future work.

Introduction

Unidirectional continuous-fiber polymer matrix composites are widely used in lightweight structural applications due to their high specific stiffness and strength and their pronounced anisotropy. Their mechanical response depends not only on nominal fiber volume fraction and layup, but also on process-induced microstructure. Relevant features include voids, resin-rich domains, fiber misalignment, fiber waviness, inter-bundle heterogeneity, and spatial variability at the roving or tape scale [1, 2, 3]. These non-idealities degrade matrix-dominated properties such as interlaminar shear strength, transverse compression resistance, and fracture toughness, and they promote localized damage initiation [4, 5]. Studies on voids show that performance depends not only on void volume fraction but also on void morphology and spatial distribution [6, 7]. This evidence motivates quantitative three-dimensional characterization rather than scalar porosity metrics alone. In addition, the realized architecture of unidirectional reinforcements often deviates from the nominal fiber direction. Misalignment and waviness arise during consolidation, impregnation, placement, and pulling operations. Under compressive loading, these defects promote micro-buckling and stability-driven failure. Reviews describe fiber waviness as a process-dependent, multiscale defect for which robust metrology and quantitative property correlation remain challenging, especially when imaging resolution does not allow fiber-by-fiber discrimination [8, 9, 10]. X-ray micro-computed tomography is widely used as a non-destructive technique for three-dimensional inspection of composite microstructures. It enables visualization and quantification of internal defects, analysis of damage and fracture mechanisms, and generation of image-based geometries for numerical modelling. Reviews on quantitative tomography highlight both the advantages of true three-dimensional morphology and spatial statistics and the limitations imposed by artefacts, resolution constraints, and quantitative uncertainty [11, 12]. Applications to fiber-reinforced laminates demonstrate the ability of micro-CT to resolve delamination and microcracking, but also reveal practical trade-offs between field of view, magnification, and detectability of fine damage features [13]. The transition from qualitative visualization to reproducible quantitative metrology requires standardized acquisition protocols and explicit quality control procedures. Industrial standards such as ASTM E1441 define general practices for computed tomography. Metrology-oriented guidelines, including VDI/VDE 2630 for CT-based dimensional measurement, specify performance verification and comparability principles [14, 15, 16]. In practice, the micro-CT analysis pipeline involves multiple parameter choices across acquisition, reconstruction, pre-processing, and feature extraction. When voxel size is on the order of several micrometers to tens of micrometers, individual fibers, matrix, and voids cannot be reliably resolved. Partial-volume effects, noise, and restricted contrast make multi-class segmentation unstable and often ill-posed. Under such conditions, segmentation-free or segmentation-light strategies have been proposed. These include structure-tensor-based approaches for estimating local anisotropy and orientation without explicit fiber identification, with explicit discussion of resolution and image-quality constraints [17, 18, 19, 20]. Image-based modelling studies further emphasize that pipeline reliability depends either on high-fidelity segmentation or on the use of robust, low-dimensional descriptors when segmentation is ambiguous, especially in multiscale architectures [21]. A recurrent limitation in composite micro-CT studies is the trade-off between spatial resolution and field of view. Voxel sizes small enough to resolve fine-scale constituents require reduced imaging volumes. Conversely, capturing representative mesostructural variability requires larger fields of view and therefore coarser voxel sizes or longer acquisition times, with direct consequences for detectability and quantitative uncertainty [22, 23]. This trade-off defines a widely used operational regime with voxel sizes on the order of 5–20 µm. In this range, micro-CT resolves mesostructural features such as rovings, resin-rich zones, coarse porosity, and roving-scale waviness, but does not allow reliable multi-phase segmentation at the fiber scale. When segmentation is feasible, void- and defect-oriented analyses are well established [6, 7]. When segmentation is unstable, however, methodological practices are less standardized. In such cases, analysis must rely on statistical and spatial descriptors extracted directly from attenuation signals, together with explicit parameter reporting, sensitivity assessment, and numerical quality control. This need is reinforced by current industrial trends. Automated layup processes may introduce defects such as wrinkles, bridging, and gap or overlap regions, which require objective structural verification [24, 25]. In liquid composite molding and related processes, permeability and impregnation quality influence porosity and heterogeneity. Experimental and numerical studies show that reinforcement architecture and modelling assumptions affect inferred permeability and predicted impregnation behavior [26, 27]. In parallel, increasing attention to sustainability and thermoplastic processing routes strengthens the demand for reproducible structural metrics that enable meaningful comparison across materials and processes [28]. Against this background, the present work addresses quantitative micro-CT characterization in the limited separability regime. It proposes a low-dimensional set of statistical and spatial descriptors computed from controlled one-dimensional intensity profiles. The descriptor set includes distributional moments and quantiles, entropy, gradient-based measures, autocorrelation-derived correlation length, spectral energy ratios, and run-length statistics. The extraction procedure is accompanied by explicit numerical quality control and parameter sensitivity analysis to ensure reproducibility. The objective is to provide a traceable attenuation-based representation of mesostructural variability that supports intra- and inter-sample comparison and for subsequent mechanical interpretation and modelling

Materials and Data

Unidirectional glass fiber–reinforced polypropylene pultruded bars are investigated. The material is manufactured at the University of Salerno using a laboratory-scale pultrusion line designed and operated in-house. The reinforcement consists of forty continuous unidirectional glass fiber tapes pre-impregnated with polypropylene. The pultrusion process produces rectangular bars with constant cross-section and nominally aligned fiber reinforcement. Five reduced-size specimens are machined from the pultruded bars for microstructural analysis. Each specimen is scanned by X-ray micro-computed tomography to characterize the internal architecture at the mesostructural scale. Micro-CT acquisitions are performed using a Rigaku CT Lab HX 130 system. Scans are conducted at an accelerating voltage of 110 kV and a tube current of 72 µA. A 0.1 mm copper filter attenuates low-energy photons and reduces beam-hardening effects. Volumes are reconstructed with an isotropic voxel size of 10.5 µm using vendor-provided reconstruction software. The reconstructed grayscale volumes are exported in .vox format, inspected using Dragonfly, and converted to 16-bit TIFF stacks for slice-wise processing and feature extraction. Acquisition and reconstruction parameters are kept constant across all specimens to ensure reproducibility and enable direct inter-scan comparison.

Methodology

Fig. 1 summarizes the proposed processing pipeline. Starting from the reconstructed micro-CT volume, a volume of interest (VOI) and a fixed line-sampling scheme are defined. One-dimensional intensity profiles are extracted slice-wise within the VOI. Structural descriptors are computed from both raw and normalized intensities. The workflow produces traceable outputs for structural characterization, quality control, and sensitivity analysis. The reconstructed datasets are converted to 16-bit grayscale image stacks and processed as volumetric arrays. Slices are ordered according to file names to preserve the physical stacking direction and to prevent index permutation. Each slice is imported as a single-channel intensity image. When multi-channel data are present, the grayscale channel is retained to ensure a scalar intensity field. Let $I_k(x,y)$ denote the intensity field of the k-th slice. The three-dimensional volume is assembled as $I(x,y,z=k)=I_k(x,y), k=1,\dots,N_z$, yielding a scalar field with dimensions (N_y,N_x,N_z). All computations use the voxel spacing provided by the micro-CT reconstruction. No interpolation or resampling is applied. The volume is stored using the native integer bit-depth to avoid unintended intensity rescaling during import. Pre-processing is intentionally minimal. Spatial filtering and denoising are not applied, as they may alter local gradients, autocorrelation structure, and high-frequency spectral content. Intensity normalization is applied only after VOI definition and is explicitly parameterized. This separation decouples acquisition-dependent intensity scaling from descriptor computation and ensures reproducible comparisons across slices and specimens.

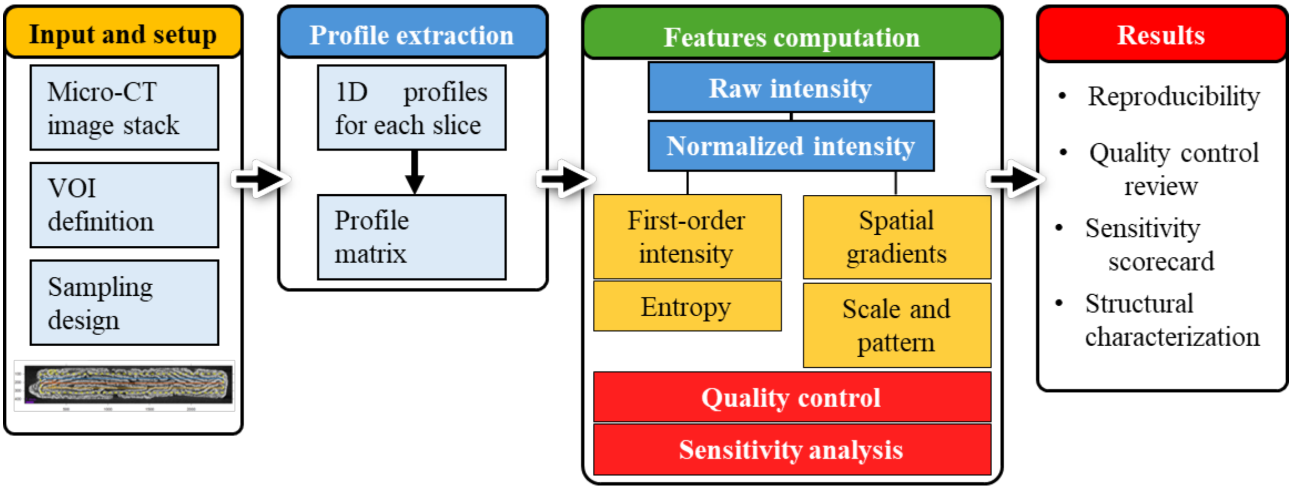

Fig. 1. Overview of the proposed micro-CT line-profile pipeline.

Processing settings and signal extraction. A three-dimensional volume of interest is defined to restrict the analysis to an internal region of the specimen. Background air and boundary zones affected by partial volume effects are excluded. The VOI is parameterized by axis aligned bounds $x_{\min}, x_{\max}$, $y_{\min}, y_{\max}$, and $z_{\min}, z_{\max}$ in the reconstructed volume coordinates. A central slice $z=k_z$ is selected as reference to define the in-plane VOI extent $[x_{\min}, x_{\max}] \times [y_{\min}, y_{\max}]$. The through-thickness extent is defined by selecting a contiguous set of slices centered on k_z. The bounds along z are set as

$$z_{\min} = \max(1, k_z - \Delta z)\,,\ z_{\max} = \min\,(N_z, k_z + \Delta z), \tag{1}$$

where Δz is the prescribed half-range expressed in number of slices and N_z is the total number of slices in the stack. This procedure yields a reproducible VOI with dimensions $(N_x^{\text{VOI}}, N_y^{\text{VOI}}, N_z^{\text{VOI}})$. To characterize spatial heterogeneity within the VOI while retaining a low dimensional representation, one-dimensional intensity profiles are sampled along the x-direction at fixed y-coordinates. Three horizontal lines $y = y_i$, with $i = 1, 2, 3$, are defined inside the VOI and uniformly spaced across the interval $[y_{min}, y_{max}]$ to probe transverse variability. For each slice $z \in [z_{\min}, z_{\max}]$, the corresponding intensity profile is extracted as

$$p_i(x; z) = I(x, y_i, z),\ \ x \in [x_{\min}, x_{\max}], \tag{2}$$

yielding a set of profiles $\{p_i(\cdot; z)\}$ of length N_x^{VOI} for each slice. This sampling strategy provides both slice wise and line wise descriptions of the attenuation signal. It enables the assessment of transverse variability and through thickness stability without requiring full three-dimensional phase segmentation. Restricting the analysis to an internal VOI reduces edge related artefacts, while fixed-y sampling ensures controlled and repeatable probing of the microstructural signal. The use of multiple equidistant line profiles enables detection of spatial non uniformity with limited additional complexity. To enable quantitative comparisons across slices and, when applicable, across specimens, grayscale intensities are transformed using a relative calibration based on two reference levels. The calibration uses a low attenuation background reference and a high intensity reference representative of the solid phase. Let $I(\mathbf{r})$ denote the reconstructed grayscale intensity at voxel location $\mathbf{r}$. The background reference g_{air} is estimated from a region selected outside the specimen and summarized using a robust statistic to limit the influence of outliers. The high intensity reference g_{ref} is defined as a high percentile P_q of the intensity distribution within the VOI, with $q = 99.5$ unless otherwise stated. This specimen specific reference provides a stable upper anchor while remaining insensitive to isolated extreme values. The use of a global VOI-based reference avoids slice wise normalization and preserves through-thickness trends. The normalized intensity field is computed through an affine transformation,

$$I_{\text{norm}}(\mathbf{r}) = \frac{I(\mathbf{r}) - g_{\text{air}}}{g_{\text{ref}} - g_{\text{air}}}, \tag{3}$$

followed, when required, by clipping to a bounded range to improve numerical stability and limit the influence of rare extreme values,

$$I_{\text{norm}}(\mathbf{r}) \leftarrow \min\,(\max\,(I_{\text{norm}}(\mathbf{r}), 0), 1). \tag{4}$$

The same transformation is applied to all extracted line profiles, yielding paired datasets of raw profiles $p_i(x; z)$ and normalized profiles $p_i^{\text{norm}}(x; z)$. Structural descriptors are computed on both representations. Raw features preserve the original reconstruction scale and remain sensitive to acquisition-dependent intensity shifts. Normalized features reduce scan to scan scaling effects and support quantitative comparison across slices and specimens. All calibration parameters g_{air}, g_{ref}, and q are recorded to ensure full traceability and reproducibility.

Feature definition. For each line profile $p_i(x; z)$ sampled along the x-direction at fixed (y_i, z), first-order descriptors are computed to summarize the marginal distribution of grayscale intensities. These descriptors are independent of the spatial ordering of samples along the profile. Let $\{x_n\}_{n=1}^{N}$ denote the N discrete intensity samples of a profile, either raw or normalized. The sample mean μ and sample standard deviation σ are defined as

$$\mu = \frac{1}{N}\sum_{n=1}^{N} x_n \text{ and } \sigma = \sqrt{\frac{1}{N-1}\sum_{n=1}^{N}(x_n - \mu)^2}. \tag{5, 6}$$

Relative dispersion is quantified using the coefficient of variation,

$$\mathrm{CV} = \frac{\sigma}{\mu}, \tag{7}$$

which is reported only when $\mu \neq 0$. Distributional asymmetry and tail behavior are characterized using central standardized moments. Skewness γ_1 and excess kurtosis γ_2 are computed as

$$\gamma_1 = \frac{\frac{1}{N}\sum_{n=1}^{N}(x_n-\mu)^3}{\sigma^3}, \text{ and } \gamma_2 = \frac{\frac{1}{N}\sum_{n=1}^{N}(x_n-\mu)^4}{\sigma^4} - 3, \tag{8, 9}$$

with $\gamma_2 = 0$ for a Gaussian distribution by construction. Robust location and scale are further described using empirical percentiles. The 10th, 50th (median), and 90th percentiles are denoted as P_{10}, P_{50}, and P_{90}, respectively. The interquartile range is defined as

$$\mathrm{IQR} = P_{75} - P_{25}. \tag{10}$$

First-order descriptors provide a compact representation of the attenuation statistics sampled along each line. They capture shifts in average intensity level, dispersion, and the presence of extreme values. Because they ignore spatial ordering, these descriptors are insensitive to the spatial arrangement of phases and therefore complement the order-dependent descriptors introduced in the following sections. To quantify distributional complexity beyond moment-based statistics, the Shannon entropy of the intensity histogram is computed for each line profile. For a given profile $\{x_n\}_{n=1}^{N}$, a discrete probability mass function is estimated by binning the samples into B fixed width bins over a prescribed intensity range. Let c_b denote the count in bin b and $p_b = c_b / \sum_{b=1}^{B} c_b$ the corresponding empirical probability. The Shannon entropy is defined as

$$H = -\sum_{b=1}^{B} p_b \log_2(p_b), \text{ with } p_b > 0. \tag{11}$$

The binning parameters are held constant within each analysis to ensure comparability across slices and lines. When normalized intensities are used, the intensity range is naturally bounded and the same binning strategy is applied. First-order statistics and histogram entropy do not account for the spatial ordering of samples along the profile. To capture spatial variability along the sampled direction, descriptors derived from the first discrete difference of the intensity signal are computed. For a profile x_n, the discrete gradient is defined as

$$\Delta x_n = x_{n+1} - x_n, n = 1, \dots, N-1. \tag{12}$$

From this gradient signal, two scalar descriptors are computed: the root-mean-square gradient magnitude and the mean absolute gradient,

$$G_{\mathrm{RMS}} = \sqrt{\frac{1}{N-1}\sum_{n=1}^{N-1}(\Delta x_n)^2}, \text{ and } G_{\mathrm{ABS}} = \frac{1}{N-1}\sum_{n=1}^{N-1} \mid \Delta x_n \mid. \tag{13, 14}$$

These descriptors increase with the amplitude and frequency of local intensity transitions along the profile and therefore provide compact proxies for edge density and fine-scale texture in the sampled direction.

To quantify the characteristic spatial scale of intensity fluctuations along each profile, an autocorrelation-based correlation length is computed. For a given line profile $\{x_n\}_{n=1}^{N}$, the mean value is first removed to suppress the DC component, $x'_n = x_n - \mu$ The normalized autocorrelation function is then evaluated for non-negative integer lags l as

$$R(\ell) = \frac{\sum_{n=1}^{N-\ell} x'_n x'_{n+\ell}}{\sum_{n=1}^{N}(x'_n)^2}, \ell = 0,1, \dots, \ell_{\max}, \tag{15}$$

with $R(0) = 1$ by construction. The correlation length $L_{\mathrm{corr,e}}$ is defined as the smallest lag $l \geq 1$ at which the autocorrelation decays below a prescribed threshold T,

$$L_{\mathrm{corr},e} = \min\{\ell \geq 1 \mid R(\ell) < T\}, \tag{16}$$

with $T = \mathrm{e}^{-1}$ unless otherwise stated. To ensure consistent behavior across profiles of different lengths and to limit computational cost, the maximum evaluated lag is capped at $l_{\max}$. If the threshold is not crossed within the interval $[1, l_{\max}]$, the correlation length is set equal to $l_{\max}$. Profiles with negligible variance, defined by $\sigma \approx 0$, are excluded from this computation. The correlation length $L_{\mathrm{corr,e}}$ estimates the typical distance, expressed in pixels, over which intensities remain correlated along the sampled direction. Larger values correspond to slowly varying profiles dominated by extended domains, whereas smaller values indicate rapid decorrelation consistent with finer-scale texture or frequent intensity transitions. To characterize the distribution of spatial frequencies in each line profile, the one-dimensional power spectrum of the mean-centered signal is analyzed. For a profile x_n, the mean-centered signal is defined as $x'_n = x_n - \mu$. Let $X(k)$ denote the discrete Fourier transform of x'_n, with $k = 0, \dots, N-1$. The one-sided power spectrum $P(f_k)$ is computed from $\mid X(k) \mid^2$ using standard one-sided scaling. The normalized spatial frequency axis is defined as

$$f_k = \frac{k}{N},\ f_k \in [0{,}0.5], \tag{17}$$

where $f = 0.5$ corresponds to the Nyquist frequency expressed in cycles per pixel. The zero-frequency component is excluded to focus on spatial variations. The total spectral energy is defined as

$$E_{\mathrm{tot}} = \sum_{f_k > 0} P(f_k). \tag{18}$$

To obtain a compact multi-scale description, the spectrum is partitioned into three non-overlapping frequency bands. Low-, mid-, and high-frequency bands are defined by two cut-off frequencies f_{low} and f_{mid}, with $0 < f_{\mathrm{low}} < f_{\mathrm{mid}} \leq 0.5$. The corresponding band energies are computed as

$$E_{\mathrm{low}} = \sum_{0 < f_k \leq f_{\mathrm{low}}} P(f_k)\ , E_{\mathrm{mid}} = \sum_{f_{\mathrm{low}} < f_k \leq f_{\mathrm{mid}}} P(f_k) \text{ and} \tag{19, 20}$$

$$E_{\mathrm{high}} = \sum_{f_{\mathrm{mid}} < f_k \leq 0.5} P(f_k). \tag{21}$$

The normalized band-energy ratios are then defined as

$$\eta_{\mathrm{low}} = \frac{E_{\mathrm{low}}}{E_{\mathrm{tot}}} \text{ and } \eta_{\mathrm{mid}} = \frac{E_{\mathrm{mid}}}{E_{\mathrm{tot}}} \text{ and } \eta_{\mathrm{high}} = \frac{E_{\mathrm{high}}}{E_{\mathrm{tot}}}, \tag{22, 23, 24}$$

which satisfy $\eta_{\mathrm{low}} + \eta_{\mathrm{mid}} + \eta_{\mathrm{high}} \approx 1$ when $E_{\mathrm{tot}} > 0$. Low-frequency energy reflects slowly varying intensity profiles dominated by large-scale domains, whereas high-frequency energy reflects rapid intensity fluctuations and fine-scale texture along the sampled direction. The cut-off frequencies f_{low} and f_{mid} control how spectral energy is redistributed among bands and therefore directly influence the resulting descriptors. These cut-offs are treated as explicit hyperparameters and their impact is quantified in the sensitivity analysis. To quantify the spatial extent and frequency of contiguous high- and low-intensity domains along each line profile, run-length descriptors based on percentile thresholds are computed. For a given profile $\{x_n\}_{n=1}^{N}$, two robust thresholds are defined from the empirical intensity distribution. The lower threshold is set to the 10th percentile $\tau_{\mathrm{lo}} = P_{10}$, and the upper threshold is set to the 90th percentile $\tau_{\mathrm{hi}} = P_{90}$. These percentiles target the distribution tails while remaining robust to isolated outliers. Two binary indicator sequences are then constructed as

$$b_n^{\mathrm{hi}} = \mathbb{I}(x_n > \tau_{\mathrm{hi}}) \text{ and } b_n^{\mathrm{lo}} = \mathbb{I}(x_n < \tau_{\mathrm{lo}}), \tag{25, 26}$$

where $\mathbb{I}(\cdot)$ denotes the indicator function. A run is defined as a maximal contiguous sequence of ones in the corresponding binary sequence. For each binary sequence, the number of runs N_{run}, the maximum run length $L_{\max}$, and the mean run length L_{mean} are computed. If no runs are present, these descriptors are set to zero. To enable comparisons across profiles of different lengths, all run-length descriptors are also reported in normalized form,

$$N_{\mathrm{run}}^{*} = \frac{N_{\mathrm{run}}}{N} \text{ and } L_{\max}^{*} = \frac{L_{\max}}{N} \text{ and } L_{\mathrm{mean}}^{*} = \frac{L_{\mathrm{mean}}}{N}. \tag{27, 28, 29}$$

High-tail run descriptors capture the occurrence and spatial persistence of contiguous high-intensity domains along the sampled direction. Low-tail run descriptors capture the occurrence and persistence of low-intensity domains. Because run formation depends explicitly on the chosen percentile thresholds, these descriptors are intrinsically sensitive to threshold selection. This dependence is addressed explicitly in the sensitivity analysis. All descriptors are computed at the profile level, that is, for each sampled line i and each slice z. This produces a long-format dataset in which each record corresponds to a unique (i, z) pair and contains the full set of feature values derived from the corresponding profile. This representation preserves slice-wise variability and provides the input for quality control and sensitivity analysis. To enable compact comparisons between transverse locations, each feature is further aggregated along the slice direction. For each line i, summary statistics over z are computed, including mean, standard deviation, median, minimum, and maximum. The resulting aggregated by line representation provides low-dimensional descriptors that summarize through-thickness variability while retaining sensitivity to persistent structural differences between lines. When required, linear trends with respect to z are estimated by least-squares fitting to quantify systematic drifts along the volume.

Quality control and sensitivity analysis. A technical quality control procedure is applied to ensure numerical validity, internal consistency, and comparability of the extracted descriptors. Control is performed at both the profile level and the aggregated by line level, and separately for raw and normalized features when both representations are available. Each feature record must correspond to a unique sampling location identified by the pair (i, z), where i denotes the line index and z the slice index within the VOI. The number of records is verified against the expected cardinality $N_{\text{lines}} \times N_z^{\text{VOI}}$. Duplicate or missing keys are not permitted. When raw and normalized tables are both present, key sets must match exactly to allow one to one alignment. For each feature, the fraction of non-finite values is quantified at the profile and aggregated levels. Concentrated missingness patterns are flagged, as they may indicate nearly constant profiles or ill-posed computations such as divisions by $\mu \approx 0$. Numerical validity is enforced by checking that all statistics satisfy their analytical prerequisites, for example $\sigma > 0$ for standardized moments. Each descriptor is checked against constraints implied by its definition. Entropy and gradient-based descriptors must be non-negative. Run counts and run lengths must be non-negative. Normalized spectral energy ratios must lie within the interval $[i, z]$. For the spectral band descriptors, approximate closure is verified,

$$\eta_{\text{low}} + \eta_{\text{mid}} + \eta_{\text{high}} \approx 1, \tag{31}$$

whenever $E_{\text{tot}} > 0$. For the autocorrelation-based correlation length, it is verified that $L_{\text{corr,e}}$ lies within the evaluated lag range$[1, l_{\max}]$ when defined. Any violation is traced back to the corresponding (i, z) key. When both raw and normalized feature tables are available, records are aligned using identical keys. The absence of mismatches is verified, and normalization is checked to ensure that it does not introduce degenerate behavior beyond the expected effects of clipping. This step ensures that intensity rescaling preserves the structural information encoded in the profiles. Several descriptors depend on explicit hyperparameters, including the autocorrelation threshold T and maximum lag $l_{\max}$, the spectral band cut-offs f_{low} and f_{mid}, the histogram bin count, and the percentile thresholds used in run-length definitions. To assess robustness with respect to these choices, a one at a time sensitivity analysis is performed. One hyperparameter group is varied while all other processing steps, including VOI definition and line sampling, are kept fixed. For each descriptor family, a baseline parameter set Θ_0 is defined. Perturbed configurations $\{\Theta_j\}$ are generated by modifying the corresponding hyperparameters within plausible ranges. Features are recomputed on the same set of sampled profiles for each configuration and compared to the baseline at both the profile level and the aggregated by line level. Robustness is quantified using three complementary metrics. First, the Spearman rank correlation between baseline and perturbed values is computed to assess preservation of relative ordering. Second, the magnitude of deviation is evaluated through the median and upper quantile of the absolute relative difference,

$$\delta = \frac{|f(\Theta_j) - f(\Theta_0)|}{|f(\Theta_0)| + \varepsilon}, \tag{32}$$

where $\varepsilon > 0$ ensures numerical stability. Third, degeneracy is monitored by tracking the variance and number of unique values under each configuration. This step identifies descriptors that collapse toward nearly constant outputs under specific parameter choices. Robustness results are summarized through a scorecard that ranks parameter configurations within each descriptor family. For each feature, a composite score combines rank preservation, deviation magnitude, and penalties for degeneracy. Scores are then aggregated across features to obtain a per-configuration robustness ranking at both representation levels. The scorecard supports transparent selection of parameter values that yield stable and reproducible descriptors. The sensitivity patterns observed in the scorecard reflect the structural role of each hyperparameter in the descriptor definition. Spectral band cut-offs directly determine how the total spectral energy is partitioned across low, mid, and high frequency ranges. Because the band-energy ratios are normalized by the same total energy, shifting the cut-off frequencies redistributes energy between bands even when the underlying spectrum remains unchanged. As a result, moderate variations in f_{low} and f_{mid} can produce non-negligible changes in the reported band ratios and in their relative ordering across profiles. Run-length descriptors exhibit stronger sensitivity because the percentile thresholds alter the binary segmentation of the intensity signal itself. Changing P_{10} or P_{90} modifies which samples are classified as tail events, thereby redefining the set of contiguous runs. Since run counts and run lengths are computed on this thresholded signal, small shifts in percentile values can induce discrete changes in run formation, leading to larger variations than those observed for moment-based or correlation-based descriptors. In contrast, autocorrelation threshold and histogram bin count affect only secondary aspects of their respective computations and do not modify the underlying signal partitioning. Their influence is therefore comparatively limited within the tested parameter ranges.

Results and Discussion

Case study. The proposed framework is applied to a representative pultruded GF/PP micro-CT volume to demonstrate end to end execution under fixed processing settings. An internal volume of interest is defined using axis-aligned bounds to exclude background and boundary regions. Within the VOI, three horizontal line profiles are sampled along the x-direction at uniformly spaced y-coordinates. The same line locations are used for all slices to ensure consistent transverse comparison and through-thickness tracking. Fig. 2 shows a representative reconstructed slice with the selected VOI and the three fixed line profiles. The VOI contains $N_z = 1931$ slices. Each line profile spans $N_x = 2190$ pixels, corresponding to a spatial length of 22.995 mm at a voxel size of 10.5 µm. The sampling scheme produces 5793 profiles per intensity domain. For each slice z, descriptors are computed from full-length profiles using both raw and normalized intensities. Unless otherwise stated, results are reported for normalized intensities to reduce scan-scale effects while preserving relative through-thickness variation. Descriptors are summarized at the line level by aggregating across z using median and interquartile range. Run-length descriptors use the 10th and 90th percentiles to define lower and upper tail thresholds.

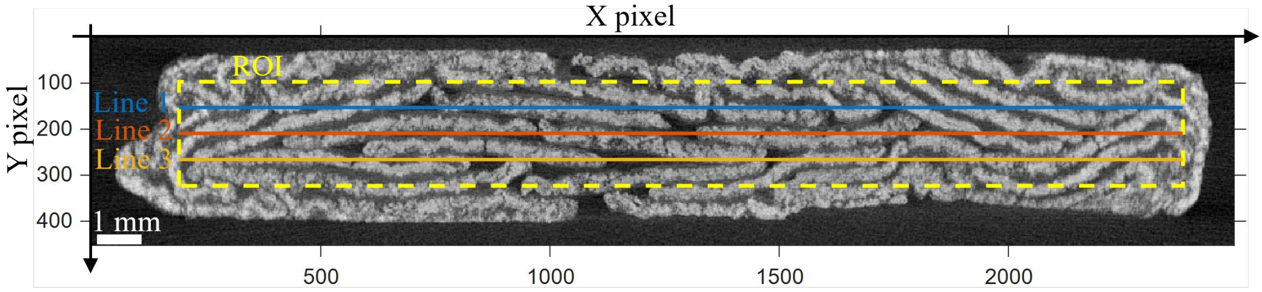

Fig. 2. Representative reconstructed slice showing the selected internal volume of interest and three uniformly spaced line profiles sampled along the x-direction.

Quality control and sensitivity analysis results. The report confirms full integrity of the extracted profile dataset. Raw and normalized outputs contain 5793 profiles each and show perfect key consistency with no missing entries in either domain. The pipeline produces complete and numerically stable features for all descriptors and no domain-constraint violations. Raw–norm consistency follows the expected behavior, scale-invariant descriptors remain unchanged while scale-dependent descriptors rescale under normalization but preserve ordering. Entropy shows a lower correlation (r = 0.869) because normalization changes the histogram support and bin occupancy, which the pipeline treats as expected. Sensitivity outcomes reveal distinct influence regimes across parameter groups. These regimes are quantified through rank correlation, relative deviation, and composite score magnitude at both aggregated and profile levels. Autocorrelation parameters and entropy bin counts show limited influence within the tested ranges. At both representation levels, Spearman rank correlation remains above 0.99 and median relative deviations remain below 0.04. Composite scores remain confined to a narrow interval between 0.10 and 0.18. These parameters modify decay threshold or histogram resolution without altering the structural partitioning of the signal. Spectral band cut-offs exhibit substantially larger deviations. For perturbed FFT configurations, relative median deviations reach values close to unity and composite scores exceed 1.5 in the most extreme cases. Rank correlation decreases to approximately 0.89 at the profile level. This behavior arises from redistribution of spectral energy across frequency bands when cut-off frequencies are modified. Because band-energy ratios are defined by energy partitioning, shifting the boundaries alters descriptor magnitudes even if the underlying spectrum remains unchanged. Run-length thresholds represent the strongest sensitivity driver. Changing percentile thresholds modifies the binary indicator sequences used to construct contiguous runs. This redefinition of the thresholded signal produces discrete changes in run topology rather than gradual magnitude shifts. At the aggregated level, composite scores exceed 1.1 and rank correlation drops below 0.5 for the most extreme threshold variation. These values are markedly higher than those observed for other descriptor families. The scorecard therefore separates parameter groups that induce smooth metric perturbations from those that alter the structural segmentation of the signal. Based on these results, the baseline configuration used for structural interpretation adopts an autocorrelation threshold $T = \mathrm{e}^{-1}$ with $l_{\max} = 100$, a 256-bin histogram discretization, spectral cut-offs at normalized frequencies 0.10 and 0.30 cycles per pixel, and run-length thresholds defined by the 10th and 90th percentile.

Structural characterization. To assess transverse uniformity within the VOI, three fixed transverse positions are sampled using line profiles oriented along the x-direction and repeated for each slice z. Fig. 3 shows a representative line profile extracted from a single slice together with the percentile thresholds used for run-length analysis. Each profile is a one-dimensional sequence of normalized voxel intensities. In micro-CT, voxel intensity reflects local X-ray attenuation. In this composite system, attenuation variations primarily reflect differences in effective density and phase composition. Higher intensity values are consistent with fiber-rich regions intersected by the sampling line. Lower intensity values are consistent with resin-rich or lower-density regions. No phase segmentation is performed. Intensity statistics are therefore treated as indirect descriptors of the spatial distribution of attenuation contrast along the sampled direction. Fig. 3 also illustrates how low-tail and high-tail runs are defined relative to percentile thresholds. Run counts and run lengths quantify the spatial persistence of extreme attenuation domains along the line.

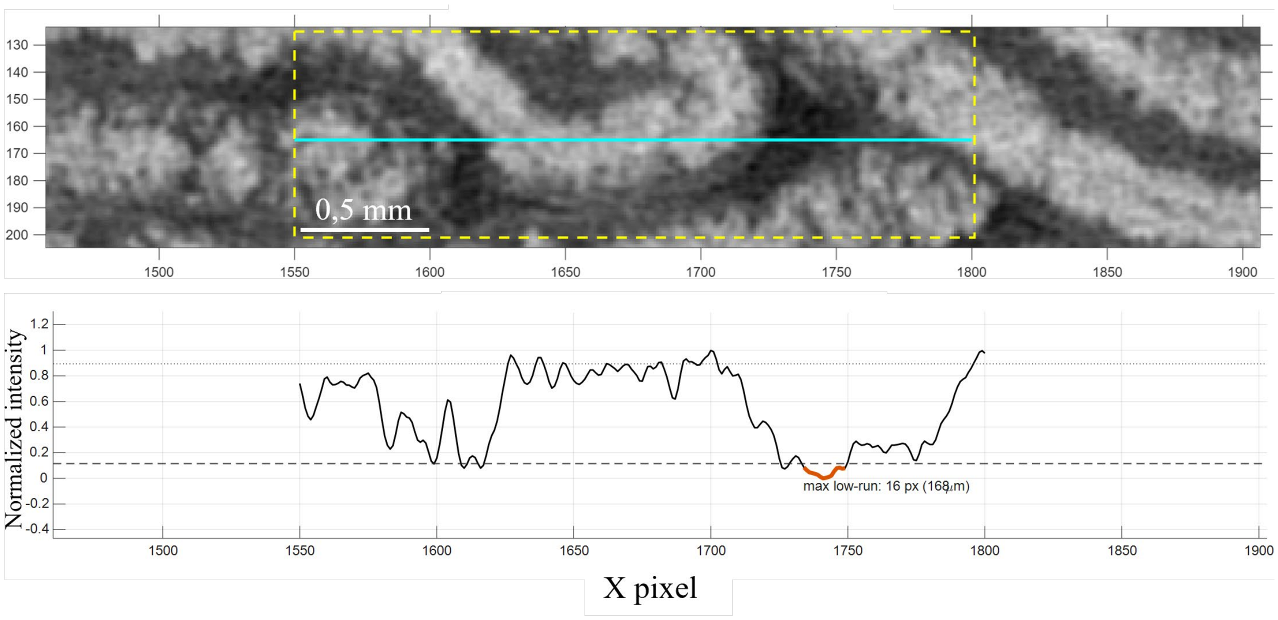

Fig. 3. Representative normalized intensity profile extracted along the x-direction within the VOI. Dashed lines indicate the 10th and 90th percentile thresholds used for run-length analysis. Highlighted segments correspond to low-tail runs.

Slice-wise descriptors are computed for each line and summarized across the VOI using median and interquartile range. Transverse comparison reveals systematic differences between the three sampled positions. The mean attenuation μ, within-profile dispersion, and correlation length $L_{\text{corr,e}}$ exhibit distinct central tendencies across lines, indicating non-uniform attenuation structure across the section. These differences are consistent with mesostructural heterogeneity at the tape or roving scale. Normalized high-frequency energy ratios and run-length descriptors further differentiate transverse locations. Lines exhibiting higher η_{high} show increased fine-scale intensity fluctuations. Lines with larger normalized low-tail run lengths exhibit more persistent low-attenuation domains. Through-thickness trends are evaluated by analyzing descriptor evolution along z. For selected lines, μ and $L_{\text{corr,e}}$ show gradual monotonic drift, indicating slow variation of attenuation structure along the stack. The largest increase in correlation length is observed for line 3 over the analyzed range. These observations indicate that fixed 1D profile descriptors capture both transverse heterogeneity and slow through-thickness modulation of attenuation structure. The descriptors provide quantitative measures of attenuation variability and spatial scale without requiring explicit phase segmentation. They allow controlled comparison of transverse positions and systematic tracking along the stack. However, intensity-based descriptors do not directly yield phase volume fractions or fiber orientation. They quantify statistical and spatial properties of the attenuation field under fixed acquisition conditions. Line sampling reduces dimensionality and does not capture full two- or three-dimensional morphology. Results may be influenced by reconstruction artefacts and partial-volume effects. Validation against independent structural or mechanical measurements remains necessary. Fig. 4 reports boxplots of slice-wise descriptor values computed from normalized line profiles. The plotted quantities are mean intensity μ, interquartile range (IQR), autocorrelation-based correlation length $L_{\text{corr,e}}$, high-frequency spectral energy ratio η_{high}, and normalized maximum low-tail run length $L^*_{\max,\text{lo}}$. Each boxplot summarizes the distribution of a descriptor across the full slice range for a fixed transverse position. Differences between lines reflect transverse heterogeneity. Spread within each box reflects through-thickness variability at that location. The mean intensity μ differs systematically across transverse positions. The central tendency of μ shows limited overlap between lines. Line 1 exhibits the highest median value, line 2 the lowest, and line 3 intermediate values. These differences indicate that the average attenuation level sampled along x varies across the section.

Lower median μ at line 2 corresponds to a higher contribution of lower-attenuation regions along that transverse location. Higher median μ at line 1 corresponds to a greater contribution of higher-attenuation regions. The interquartile range quantifies the spread of intensity values along each profile. Line 3 exhibits higher median IQR values compared to lines 1 and 2, indicating stronger intensity contrast along x at that transverse position. Line 2 shows a broader slice-wise distribution of IQR values, indicating larger through-thickness variability in local heterogeneity at that location. This suggests that the attenuation structure sampled at line 2 varies more strongly along z than at the other transverse positions. The autocorrelation-based correlation length $L_{\mathrm{corr,e}}$ increases progressively from line 1 to line 3 with limited overlap between distributions. Because $L_{\mathrm{corr,e}}$ estimates the spatial scale over which intensities remain correlated, larger values correspond to more slowly varying profiles along x. The observed increase from line 1 to line 3 therefore indicates a transverse shift toward larger-scale attenuation domains at line 3. The normalized high-frequency energy ratio η_{high} quantifies the fraction of spectral energy located in the high-frequency band. Larger values indicate stronger rapid intensity fluctuations along the sampled direction. Line 2 exhibits the highest median η_{high}. Lines 1 and 2 display heavier upper tails compared to line 3, indicating the presence of slices with locally enhanced fine-scale fluctuations. The normalized maximum low-tail run length $L^{*}_{\mathrm{max,lo}}$ measures the longest contiguous segment of low-intensity values along a profile, expressed relative to profile length. This descriptor quantifies the spatial persistence of low-attenuation domains. Line 2 shows the highest median $L^{*}_{\mathrm{max,lo}}$, indicating more persistent low-attenuation segments at that transverse position. Line 3 exhibits fewer low-tail events overall but occasional longer excursions, consistent with a broader upper spread in the corresponding boxplot. Across all descriptors, the attenuation field within the VOI is not transversely uniform. The three sampled positions exhibit distinct combinations of average attenuation level, within-profile dispersion, correlation length, high-frequency spectral content and persistence of low-attenuation domains. These differences are consistent with mesostructural heterogeneity across the section at the sampling scale considered. Through-thickness trends are evaluated by fitting slice-wise descriptor values as a function of z for each transverse line. Slopes are estimated using block-bootstrap confidence intervals to account for serial dependence along the stack. Line 2 exhibits a consistent drift pattern. The mean attenuation μ increases with z, while IQR and $L_{\mathrm{corr,e}}$ decrease. In parallel, η_{high} and $L^{*}_{\mathrm{max,lo}}$ show positive slopes. This combination indicates a progressive shift toward shorter correlation lengths and increased persistence of low-attenuation segments along the stack. Line 3 exhibits a different trend. The mean attenuation decreases with z, while the correlation length increases. This behaviour indicates a shift toward more slowly varying attenuation profiles along the sampled direction. These results demonstrate that slice-wise descriptors detect systematic attenuation changes along the stack, in addition to transverse heterogeneity across the section.

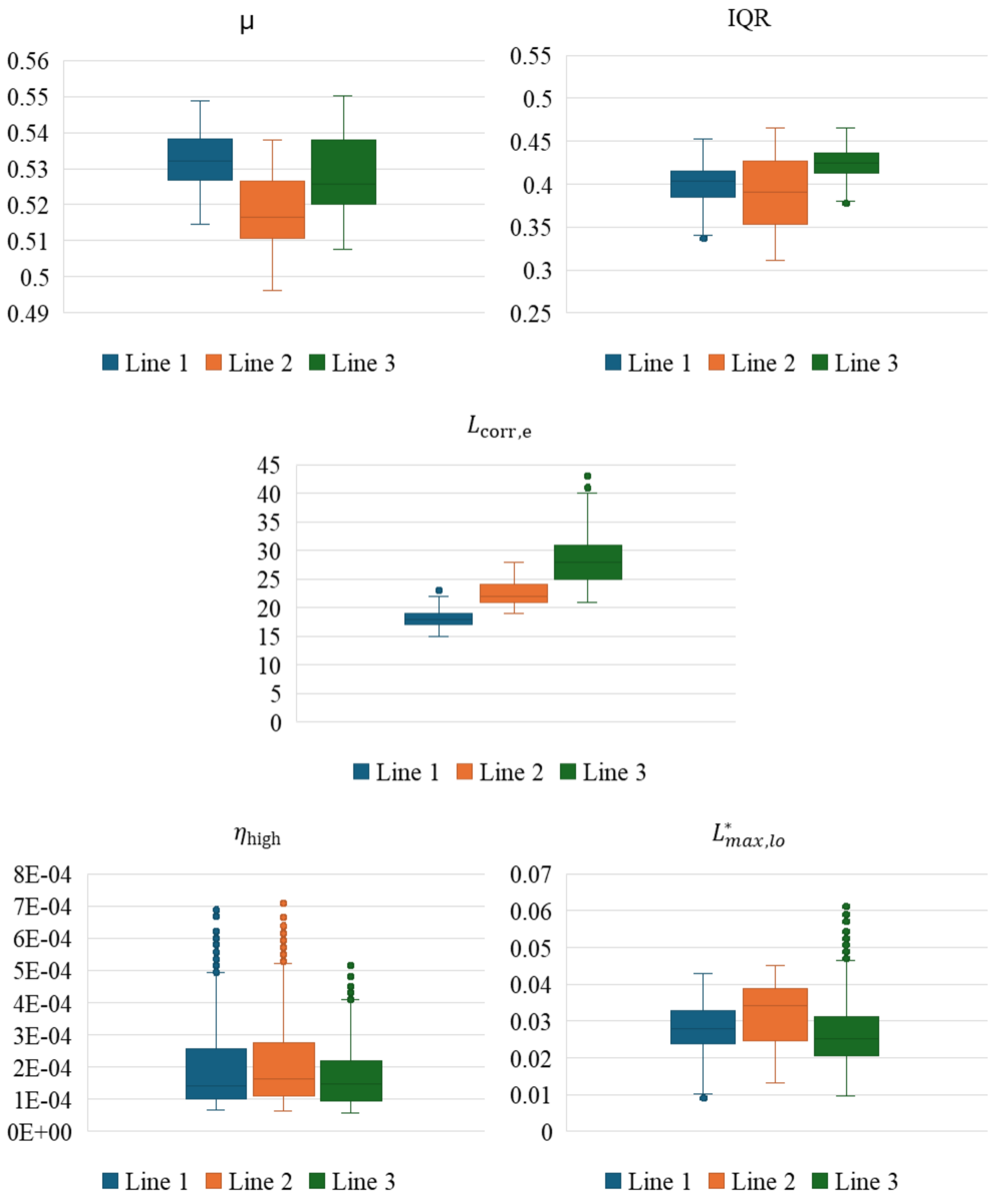

Fig. 4. Boxplots of slice-wise descriptor values computed from normalized profiles at three transverse positions. Boxes represent median and interquartile range. Whiskers extend to 1.5×IQR. Points denote outliers.

Conclusions

This study establishes a reproducible descriptor-based representation of attenuation structure in unidirectional pultruded composites directly from micro-CT intensity profiles, without relying on explicit phase segmentation. The extracted line-profile descriptors resolve measurable transverse heterogeneity across the section. Mean attenuation separates transverse locations with limited overlap. Within-profile dispersion and spectral content reveal line-dependent differences in fine-scale variability. The autocorrelation-based correlation length identifies systematic transitions in characteristic spatial scale across the section. Run-length descriptors quantify the persistence of low-attenuation domains and distinguish transverse regions through differences in contiguous segment length. Slice-wise analysis further reveals coherent through-thickness trends. Selected descriptors exhibit monotonic drifts along the stack, demonstrating that low-dimensional intensity-based metrics detect organized structural modulation rather than purely stochastic slice-to-slice fluctuation. Quality control confirms numerical completeness and internal consistency of the descriptor tables. Sensitivity analysis quantitatively separates weakly influential parameter groups from structurally influential ones. Autocorrelation and entropy settings show limited impact within the tested ranges, whereas spectral band limits and percentile thresholds materially affect descriptor magnitude and ordering. This establishes a transparent parameter policy for reproducible reporting. The principal output of the work is therefore a compact, traceable set of mesostructural indicators that quantify attenuation level, dispersion, spatial scale, fine-scale fluctuation intensity, and persistence of low-attenuation domains at fixed transverse positions. Future work will focus on integrating these descriptors into Abaqus-based finite-element workflows. In that context, slice-wise or aggregated descriptor fields can be mapped onto spatially varying material parameters using field-dependent properties or user-defined material subroutines. This will enable variability-aware simulations in which CT-derived structural indicators inform effective property distributions, without requiring full three-dimensional phase reconstruction. Mechanical validation and calibration of descriptor–property relationships will be addressed in subsequent studies.

Acknowledgments

This work was supported by the Ministero dell'Istruzione, dell'Università e della Ricerca, PRIN2022: Recycling of plastic wastes integrating extrusion and additive manufacturing techniques (RELIVE), code 2022FBB37P, CUP: D53D23003520006.

References

[1] D. Wilhelmsson, R. Gutkin, F. Edgren, and L. E. Asp, "An experimental study of fibre waviness and its effects on compressive properties of unidirectional NCF composites," *Compos. Part A Appl. Sci. Manuf.*, vol. 107, pp. 665–674, Apr. 2018, doi: 10.1016/j.compositesa.2018.02.013.

[2] A. S. Mahmood, J. Summerscales, and M. N. James, "Resin-Rich Volumes (RRV) and the Performance of Fibre-Reinforced Composites: A Review," *Journal of Composites Science*, vol. 6, no. 2, p. 53, Feb. 2022, doi: 10.3390/jcs6020053.

[3] M. Mehdikhani, L. Gorbatikh, I. Verpoest, and S. V. Lomov, "Voids in fiber-reinforced polymer composites: A review on their formation, characteristics, and effects on mechanical performance," May 01, 2019, *SAGE Publications Ltd*. doi: 10.1177/0021998318772152.

[4] Y. Fu and X. Yao, "A review on manufacturing defects and their detection of fiber reinforced resin matrix composites," *Composites Part C: Open Access*, vol. 8, p. 100276, Jul. 2022, doi: 10.1016/j.jcomc.2022.100276.

[5] I. Baran, I. Straumit, O. Shishkina, and S. V. Lomov, "X-ray computed tomography characterization of manufacturing induced defects in a glass/polyester pultruded profile," *Compos. Struct.*, vol. 195, pp. 74–82, Jul. 2018, doi: 10.1016/j.compstruct.2018.04.030.

[6] M. Mehdikhani, I. Straumit, L. Gorbatikh, and S. V. Lomov, "Detailed characterization of voids in multidirectional carbon fiber/epoxy composite laminates using X-ray micro-computed tomography," *Compos. Part A Appl. Sci. Manuf.*, vol. 125, Oct. 2019, doi: 10.1016/j.compositesa.2019.105532.

[7] M. Elkolali, L. P. Nogueira, P. O. Rønning, and A. Alcocer, “Void Content Determination of Carbon Fiber Reinforced Polymers: A Comparison between Destructive and Non-Destructive Methods,” *Polymers (Basel).*, vol. 14, no. 6, Mar. 2022, doi: 10.3390/polym14061212.

[8] M. P. Alves, C. A. Cimini Junior, and S. K. Ha, “Fiber waviness and its effect on the mechanical performance of fiber reinforced polymer composites: An enhanced review,” Oct. 01, 2021, *Elsevier Ltd*. doi: 10.1016/j.compositesa.2021.106526.

[9] M. R. Wisnom, “The Effect of Fibre Waviness on the Relationship between Compressive and Flexural Strengths of Unidirectional Composites,” *J. Compos. Mater.*, vol. 28, no. 1, pp. 66–76, Jan. 1994, doi: 10.1177/002199839402800105.

[10] P. Kulkarni, K. D. Mali, and S. Singh, “An overview of the formation of fibre waviness and its effect on the mechanical performance of fibre reinforced polymer composites,” Oct. 01, 2020, *Elsevier Ltd*. doi: 10.1016/j.compositesa.2020.106013.

[11] P. J. Withers *et al.*, “X-ray Computed Tomography.”

[12] Y. Gao, W. Hu, S. Xin, and L. Sun, “A review of applications of CT imaging on fiber reinforced composites,” *J. Compos. Mater.*, vol. 56, no. 1, pp. 133–164, Jan. 2022, doi: 10.1177/00219983211050705.

[13] P. J. Schilling, B. P. R. Karedla, A. K. Tatiparthi, M. A. Verges, and P. D. Herrington, “X-ray computed microtomography of internal damage in fiber reinforced polymer matrix composites,” *Compos. Sci. Technol.*, vol. 65, no. 14, pp. 2071–2078, Nov. 2005, doi: 10.1016/j.compscitech.2005.05.014.

[14] E. A. Zwanenburg, M. A. Williams, and J. M. Warnett, “Performance testing of dimensional X-ray computed tomography systems,” *Precis. Eng.*, vol. 77, pp. 179–193, Sep. 2022, doi: 10.1016/j.precisioneng.2022.05.005.

[15] “Guide for Computed Tomography (CT) Imaging,” Jul. 01, 2019, *ASTM International, West Conshohocken, PA*. doi: 10.1520/E1441-19.

[16] “DIN EN ISO 10360-7:2011-09, Geometrische Produktspezifikation (GPS)_- Annahme- und Bestätigungsprüfung für Koordinatenmessgeräte (KMG)_- Teil_7: KMG mit Bildverarbeitungssystemen (ISO_10360-7:2011); Deutsche Fassung EN_ISO_10360-7:2011,” Sep. 2011, *DIN Media GmbH, Berlin*. doi: 10.31030/1726376.

[17] R. Karamov, L. M. Martulli, M. Kerschbaum, I. Sergeichev, Y. Swolfs, and S. V. Lomov, “Micro-CT based structure tensor analysis of fibre orientation in random fibre composites versus high-fidelity fibre identification methods,” *Compos. Struct.*, vol. 235, Mar. 2020, doi: 10.1016/j.compstruct.2019.111818.

[18] N. Jeppesen, L. P. Mikkelsen, A. B. Dahl, A. N. Christensen, and V. A. Dahl, “Quantifying effects of manufacturing methods on fiber orientation in unidirectional composites using structure tensor analysis,” *Compos. Part A Appl. Sci. Manuf.*, vol. 149, Oct. 2021, doi: 10.1016/j.compositesa.2021.106541.

[19] R. Blanc, C. Germain, J. P. Da Costa, P. Baylou, and M. Cataldi, “Fiber orientation measurements in composite materials,” *Compos. Part A Appl. Sci. Manuf.*, vol. 37, no. 2, pp. 197–206, Feb. 2006, doi: 10.1016/j.compositesa.2005.04.021.

[20] M. Krause, J. M. Hausherr, B. Burgeth, C. Herrmann, and W. Krenkel, “Determination of the fibre orientation in composites using the structure tensor and local X-ray transform,” *J. Mater. Sci.*, vol. 45, no. 4, pp. 888–896, Feb. 2010, doi: 10.1007/s10853-009-4016-4.

[21] D. He *et al.*, “Multiscale image-based modelling of composite materials,” Dec. 01, 2025, *SAGE Publications Inc.* doi: 10.1177/09506608251363653.

[22] P. Galvez-Hernandez, R. Smith, K. Gaska, M. Mavrogordato, I. Sinclair, and J. Kratz, "The effect of X-ray computed tomography scan parameters on porosity assessment of carbon fibre reinfored plastics laminates," *J. Compos. Mater.*, vol. 57, no. 29, pp. 4535–4548, Dec. 2023, doi: 10.1177/00219983231209383.

[23] J. M. Sietins, W. H. Green, and J. S. Jones, "Materials Evaluation Using X-ray Computed Tomography," in *Comprehensive Structural Integrity*, Elsevier, 2023, pp. 159–199. doi: 10.1016/B978-0-12-822944-6.00038-4.

[24] A. Gambardella, V. Esperto, F. Tucci, and P. Carlone, "Defects Reduction in the Robotic Layup Process," in *Key Engineering Materials*, Trans Tech Publications Ltd, 2022, pp. 1437–1444. doi: 10.4028/p-7v9349.

[25] V. Esperto, A. Gambardella, G. Pasquino, F. Tucci, M. Durante, and P. Carlone, "Modeling and simulation of the robotic layup of fibrous preforms for liquid composite molding," in *ESAFORM 2021 - 24th International Conference on Material Forming*, PoPuPS (University of LiFge Library), 2021. doi: 10.25518/esaform21.475.

[26] J. S. U. Schell, M. Renggli, G. H. van Lenthe, R. Müller, and P. Ermanni, "Micro-computed tomography determination of glass fibre reinforced polymer meso-structure," *Compos. Sci. Technol.*, vol. 66, no. 13, pp. 2016–2022, Oct. 2006, doi: 10.1016/j.compscitech.2006.01.003.

[27] V. Esperto, L. Boccarusso, M. Durante, L. Carrino, and P. Carlone, "Permeability analysis of natural and artificial fiber textiles for liquid composite molding process," in *Procedia Manufacturing*, Elsevier B.V., 2020, pp. 435–439. doi: 10.1016/j.promfg.2020.04.328.

[28] P. De Sio, M. Gaito, V. Esperto, E. Cozzolino, A. Astarita, and F. Tucci, "Life Cycle Assessment of a Composite Prototype Battery Enclosure for Electric Vehicles," *Sustainability (Switzerland)*, vol. 17, no. 4, Feb. 2025, doi: 10.3390/su17041579.